Low-bias negative differential resistance in graphene nanoribbon superlattices

Gerson J. Ferreira, Michael N. Leuenberger, Daniel Loss, and J. Carlos Egues

Low Bias Negative Differential Resistance in Graphene Nanoribbon Superlattices

Gerson J. Ferreira,[1,2] Michael N. Leuenberger,[2] Daniel Loss,[3] J. Carlos Egues[1,3]

[1]*Departamento de Física e Informática, Instituto de Física de São Carlos,*
Universidade de São Paulo, 13560-970 São Carlos, São Paulo, Brazil
[2]*NanoScience Technology Center and Dept. of Physics, University of Central Florida,*
12424 Research Parkway Suite 400, Orlando, FL 32826, USA
[3]*Department of Physics, University of Basel, Klingelbergstrasse 82, 4056 Basel, Switzerland*

We theoretically investigate negative differential resistance (NDR) for ballistic transport in semi-conducting armchair graphene nanoribbon (aGNR) superlattices (5 to 20 barriers) at low bias voltages $V_{\rm SD} < 500$ mV. We combine the graphene Dirac hamiltonian with the Landauer-Büttiker formalism to calculate the current $I_{\rm SD}$ through the system. We find three distinct transport regimes in which NDR occurs: (i) a "classical" regime for wide layers, through which the transport across bandgaps is strongly suppressed, leading to alternating regions of nearly unity and zero transmission probabilities as a function of $V_{\rm SD}$ due to crossing of bandgaps from different layers. (ii) a quantum regime dominated by superlattice miniband conduction, with current suppression arising from the misalignment of miniband states with increasing $V_{\rm SD}$; and (iii) a Wannier-Stark ladder regime with current peaks occurring at the crossings of Wannier-Stark rungs from distinct ladders. We observe NDR at voltage biases as low as 10 mV with a high current density, making the aGNR superlattices attractive for device applications.

I. INTRODUCTION

Graphene[1–3] has attracted much attention due to the possibility of new devices which may surpass its semiconductor counterparts in both speed and reduced power consumption[4]. This is expected due to the unique properties of graphene, e.g., the high mobility of carriers, which can lead to high current densities, and the tunability of the bandgap. Additionally, building devices on the surface could facilitate optical absorption and emission. Particularly, negative differential resistance (NDR) is essential for many applications[5–8]. In semiconductor resonant tunneling diodes[9–11] and superlattice structures[12,13], NDR is based on Fabry-Pérot type interferences arising from the impedance mismatch between the various layers. These semiconductor NDR systems can also show interesting phenomena, such as intrinsic bistability due to charge accumulation[14]. Pursuing the recent interest in graphene superlattices transport and thermal properties[15–24], it is a natural question to ask whether a graphene superlattice could exhibit similar features.

The occurrence of Klein tunneling in graphene[2] should be an obstacle to the NDR effect, as it gives a monotonically increasing contribution to the current. Narrow graphene nanoribbons overcome this limitation as the lateral confinement quantizes the Dirac cone into few-eV-wide bands. Tight-binding calculations show that it is possible to find NDR in these narrow nanoribbons at high bias voltages, 1 to 2 V[29,30]. However, for integrated circuits a low bias mV regime is desirable to reduce power consumption[46]. Low bias NDR can also be achieved in other graphene and bilayer graphene systems[31–33].

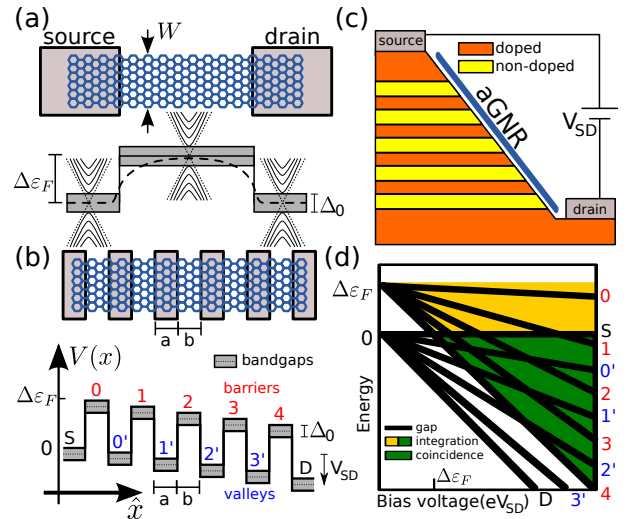In this work we consider an N-barrier superlattice potential on a semiconducting armchair graphene nanorib-

FIG. 1: [Color online] (a) Metal–aGNR junctions and the modulated chemical shift $\Delta\varepsilon_{\rm F}$ of the Dirac point across the aGNR[25–28]. Δ_0 (shaded regions) denotes the barrier and valley bandgaps. Here we consider square potentials, solid line. The dashed line shows the numerical results of Ref. 27. (b) Additional electrodes modulate the Dirac cone shift into a superlattice potential. The bias voltage $V_{\rm SD}$ is also shown. (c) Doped layers of a semiconductor superlattice can also modulate the local potential. (d) Schematic of the $\varepsilon - V_{\rm SD}$ diagram of the source–drain transmission coefficient showing crossings of the bandgaps Δ_0 (black lines). The shaded regions delimit the energy range between the source $\mu_{\rm S} = \Delta\varepsilon_{\rm F}$ and drain $\mu_{\rm D} = \mu_{\rm S} - eV_{\rm SD}$ chemical potentials.

bon (aGNR), Fig. 1. The electronic structure of the aGNR is a quantized Dirac cone, due to the quantization of the transversal momentum k_n, and can be metallic, $k_{n_0} = 0$, or semiconducting, $k_{n_0} \neq 0$, depending
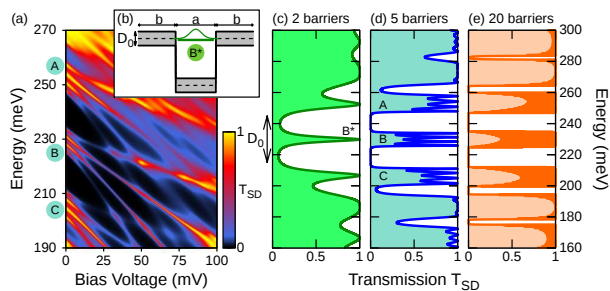
FIG. 2: [Color online] (a) Energy-voltage diagram of T_{SD} for $N = 5$ barriers showing the evolution of the $N - 1$ hybridized modes [panels (b)-(d)] into Wannier-Stark ladders. Labels A, B, and C show the zero-bias hybridized modes in panels (a) and (c). Crossings of ladders' rungs from distinct minibands increases T_{SD} near $V_{SD} = 30$ and 50 mV. (b) Schematic of the modulated Dirac point (dashed line), bandgaps $\Delta_0 \sim 28$ meV (gray area), and confined mode B'. In the transmission coefficient T_{SD} across two barriers ($a = b = 50$ nm) (c), the confined mode B' shows up as a resonant spike near 230 meV. For (d) $N = 5$, and (e) $N = 20$ barriers the confined modes hybridize into $N - 1$ spikes, building up a miniband. Similar resonances lead to minibands at energies away from the bandgap region Δ_0.

on the width W of the nanoribbon; k_{n_0} is the closest to zero transverse momenta. We choose $W = 346a_0$, such that the aGNR is semiconducting with a bandgap $\Delta_0 = 28$ meV; $a_0 = 0.142$ nm is the C-C distance. We use the transfer matrix formalism to calculate the source–drain transmission coefficient T_{SD} across the superlattice potential along the aGNR, considering a finite bias voltage V_{SD}, revealing the electronic structure of the system, Fig. 2. The potential drop from source to drain follows a piecewise constant profile layer by layer, Fig. 1(b). The current is calculated within the usual Landauer-Büttiker formalism.

We find low bias NDR at zero and room temperatures within three distinct physical regimes. (i) For wide layers, the transmission across the bandgaps Δ_0 is strongly suppressed, and nearly unity for energies away from the bandgaps. With increasing voltage, both barrier and valley bandgaps split and cross as shown schematically in Fig. 1(d), showing, at the coincidence region, a pattern of diamond shaped structures with alternating regions of finite and suppressed transmission, thus leading to NDR. For narrow barriers resonant tunneling across layers become relevant. (ii) At zero bias, hybridization of resonant modes leads to minibands with finite, nearly unity, transmission, Fig. 2(b)-(e). At very low voltages $eV_{SD} \sim 10$ meV (of the order of the miniband energy width) the resonant states misalign, thus breaking the minibands into off-resonance Wannier-Stark ladders with suppressed transmission. This gives rise to a single current spike near $eV_{SD} \sim 10$ meV. (iii) With increasing eV_{SD}, rungs of ladders from distinct minibands cross and hybridize, showing a new set of resonant spikes in T_{SD}, Fig. 2(a), thus leading to current spikes and NDR.

II. PROPOSED SYSTEM & MODEL

The modulation of the Dirac cone into a superlattice potential can be achieved by different setups. It was shown that local charge transfer effects between graphene and some metals (e.g.: Al, Cu, Ag, Au, Pt) rigidly shifts the Dirac cone[25–28], Fig. 1(a). A series of metallic stripes over graphene can create the proposed superlattice potential, Fig. 1(b). Equivalently, the same structure can be obtained by selectively doping graphene regions in an alternate fashion. Additionally, the aGNR could be arranged along the doped/non–doped layers of a clived semiconductor heterostructure[34], Fig. 1(c). Narrow systems ($\lesssim 400$ nm) are desirable to keep transport ballistic at room temperatures.

We consider low–energy excitations of graphene within the envelope function approximation[3,35], i.e., the graphene Dirac hamiltonian. The finite size of the nanoribbon requires vanishing wave-functions at the edges, where for aGNR both A and B sublattices of the honeycomb lattice are present. This leads to vanishing boundary conditions for the envelope functions at these edges[3]. The validity of these boundary conditions is discussed in Ref. 36. Within this description, the electronic structure of an aGNR is a quantized Dirac-cone, $\varepsilon = s\hbar v_f \sqrt{k_x^2 + k_n^2}$. Here $s = \pm 1$ for the conduction and valence bands, $v_f \approx 10^{15}$ nm/s is the Fermi velocity, k_x is the momentum in the longitudinal direction $\hat{x}$, $k_n = n\pi/W - 4\pi/3a_0$ is the quantized transverse momentum with integer n, and $W = 346a_0 \sim 50$ nm. The fundamental gap is given by $\Delta_0 = 2\hbar v_f |k_{n_0}| = 28$ meV, with $k_{n_0} \sim -0.021$ nm^{-1}.

To calculate the transmission $T_{SD} \equiv T_{SD}(\varepsilon, k_n, V_{SD})$ we use the transfer matrix formalism[37], which relates the coefficients of the incoming and outgoing plane waves at the source and drain leads across the superlattice layers (See Appendix for details). We consider a piecewise constant superlattice potential along the x direction, Figs. 1(b), through which the electronic structure of each layer is shifted by the local potential. In Figs. 2-4 we show T_{SD} only for k_{n_0}, as it contains the major contribution for the current in all investigated cases.

The current density of Dirac electrons in graphene is given by $\vec{j}(\mathbf{r}) = 4ev_f \psi^\dagger(\mathbf{r})\vec{\sigma}\psi(\mathbf{r})$, where the factor of 4 accounts for the valley and spin degeneracies, $\psi(\mathbf{r})$ is the envelope function spinor for the K or K' valley, and $\vec{\sigma} = (\sigma_x, \sigma_y)$ are the Pauli matrices. Within the Landauer-Büttiker formalism[37,38], the current reads

$$I_{SD} = \frac{e}{h} \sum_n \int_{-\infty}^{\infty} T_{SD}(\varepsilon, k_n, V_{SD}) \left[f_S(\varepsilon) - f_D(\varepsilon) \right] d\varepsilon, \quad (1)$$

where $f_S(\varepsilon) = \{1 + exp[(\varepsilon - \mu_S)/k_B T]\}^{-1}$ and $f_D(\varepsilon) = f_S(\varepsilon + V_{SD})$ are the Fermi-Dirac distributions at the source and drain, and μ_S is the source chemical potential. We truncate the sum over n to a few k_n near k_{n_0}.
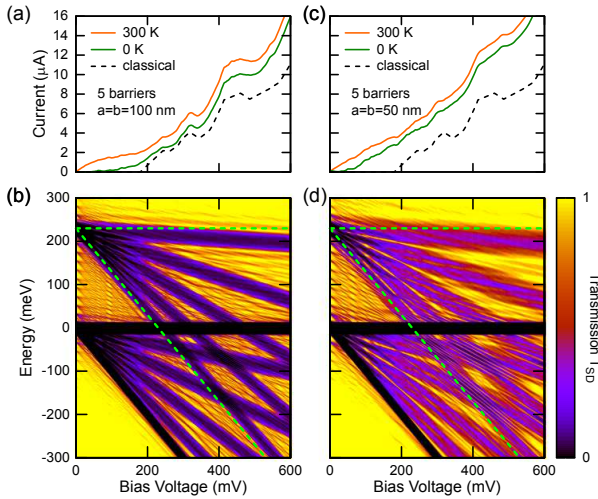
FIG. 3: [Color online] Current and energy-voltage diagram of the transmission coefficient for 5 barriers superlattice with $a = b = 100$ nm [(a) & (b)] and $a = b = 50$ nm [(c) & (d)]. The current-voltage characteristics are shown for $T = 300$ K and 0 K. For wide barriers (a)-(b) the current follows closely the limiting "classical" case of T_{SD} either 0 across bandgaps, or 1 otherwise (dashed line).

III. RESULTS

In Fig. 2(b) we consider a narrow graphene well with $a = 50$ nm and $b \to \infty$. The solution of the graphene Dirac equation within the bandgap Δ_0 region shows a confined state[39]. This state corresponds to the resonant spike within the Δ_0 region in Fig. 2(b) for 2 barriers. For N barriers the confined states hybridizes into $N - 1$ states, leading to minibands for large N, Figs. 2(c) and (d). The minibands away from the Δ_0 region occur due to reflections at each interface. For finite bias the minibands break into single resonant levels, Wannier-Stark ladders, as the confined modes from each layer misalign, Fig. 2(e). At the crossings of Wannier-Stark ladders from distinct minibands the transmission increases due to resonant tunneling.

NDR regimes

To contrast distinct NDR regimes in our system, we discuss the current-voltage characteristics I–V_{SD} and the energy–voltage T_{SD} diagram for the following three cases. We compare 5-barrier superlattices with (i) wide layers [Fig. 3(a)-(b)] and (ii) narrow layers [Fig. 3(c)-(d)]. We then discuss (iii) a 20-barrier superlattice with narrow layers, Fig. 4. The dashed lines in the T_{SD} diagrams delimit the zero temperature window of integration for I_{SD}, defined between the source $\mu_S = 230$ meV and drain $\mu_D = \mu_S - V_{SD}$ chemical potentials.

1. "Classical" regime

For wide layers, $a = b = 100$ nm, tunneling across bandgaps is strongly suppressed and the T_{SD} diagram, Fig. 3(b), follows closely the diamond pattern in Fig. 1(d). For $eV_{SD} \lesssim \Delta\varepsilon_F = 230$ meV the current increases monotonically as the barriers bandgaps misalign. At the coincidence region, $eV_{SD} \gtrsim \Delta\varepsilon_F = 230$ meV, crossings of barrier and valley bandgaps lead to the diamond pattern of finite and suppressed T_{SD}. This alternation leads to the NDR near $V_{SD} = 350$ and 450 mV, in Fig. 3(a). The intensity of the NDR in this regime increases with the layers width, as the tunneling across bandgaps becomes more suppressed. The dashed curve in Fig. 3(a) is calculated with the limiting case where tunneling is completely suppressed across bandgaps, i.e.: $T_{SD}^{classical} = 0$ across a bandgap, and 1 otherwise. Note the similarity of the dashed "classical" line with the exact I_{SD} calculations in Fig. 3(a).

For narrow layers, $a = b = 50$ nm in Fig. 3(c)-(d), the NDR due to "classical" regime is absent as it requires strong tunneling suppression. Interestingly, however, the T_{SD} diagram of a few narrow layers clearly shows the evolution of the zero-bias minibands into Wannier-Stark ladders with increasing V_{SD}, Fig. 2(e). The Wannier-Stark ladders remain as individual transmission spikes while there is an overlap of barriers (or valley) bandgaps. For $eV_{SD} > (N - 1/2)\Delta_0$ this condition is violated, and the tunneling across individual bandgaps dominate. At the crossings of barrier and valley bandgaps, resonant effects are still visible in the T_{SD} diagram as stripes, corresponding to confined states between the overlapping bandgaps, see Fig. 3(d) near $\varepsilon = -50$ meV and $V_{SD} = 400$ mV.

2. Miniband regime

Considering a larger number of barriers, $N = 20$ in Fig. 4, the aligned resonant modes hybridize into superlattice minibands, Fig. 2. If μ_S is located within the miniband, at low biases the current is dominated by the transmission across these resonant modes. As the bias increases, the modes misalign breaking up the miniband into Wannier-Stark ladders. For 5 barriers, Fig. 2(a), the rungs of the ladders shows non-resonant transmission peaks, and enhanced resonant transmission at crossings of the rungs [see *Wannier-Stark ladder regime* below]. For 20 barriers, transmission through non-resonant rungs is strongly suppressed due to the larger number of bandgaps. At very low voltages, Fig. 4, the current initially increases with V_{SD} as the transport occurs through the miniband. Near $eV_{SD} \sim 10$ meV (of the order of the miniband width) the miniband breaks up into the non-resonant rungs suppressing the current, thus resulting in a pronounced current peak.
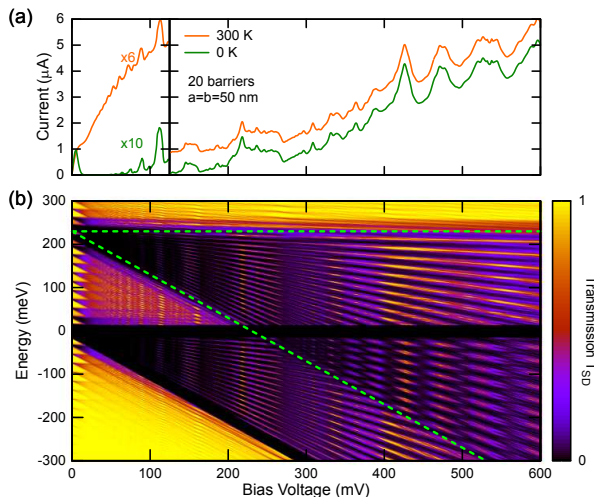
FIG. 4: [Color online] (a) Current-voltage characteristics and (b) T_{SD} diagram of a 20-barrier aGNR superlattice with $a = b = 50$ nm. In (a) the currents for 0 and 300 K in the range $0 \leq V_{SD} \leq 125$ mV are multiplied by 6 and 10, respectively, for clarity. As the voltage increases the miniband near 230 meV, Fig. 2(e), breaks up as the resonant levels misalign, leading to the pronounced spike near 10 mV for 0 K. Near 50 mV the resonant levels return as resonant crossings of Wannier-Stark ladder rungs [see also Fig. 2(a)]. At the crossings T_{SD} increases, showing current spikes at both 0 and 300 K for $V_{SD} < 230$ mV. For $V_{SD} > 230$ mV the current spikes arise from crossings of rungs at the coincidence region.

3. Wannier-Stark ladder regime

With increasing bias, rungs from Wannier-Stark ladders of distinct minibands cross, Fig. 2(a), creating new resonances through the superlattice layers. For 20 barriers, where transmission from non-resonant rungs is strongly suppressed, the crossings show sharp T_{SD} stripes, e.g., at $V_{SD} = 75$, 110, 150, and 210 mV, Fig. 4(b). Each of these stripes, and others with lower contrast at smaller voltages, leads to current spikes in Fig. 4(a). The spikes broaden with increasing bias as the bandgaps misalign. For $eV_{SD} > \Delta\varepsilon_F = 230$ meV, the crossings of broadened Wannier-Stark ladders from minibands near the barrier and valley bandgaps show diamond-shaped structures in the T_{SD} diagram, thus leading to a series of NDR spikes similar to the classical regime.

IV. CONCLUSIONS

We have found that three distinct regimes can lead to NDR in semiconducting aGNR superlattices. (i) In the "classical" regime the NDR occurs as the bandgaps of different layers cross with increasing V_{SD}. (ii) For narrow layers and very low biases, $eV_{SD} \sim 10$ meV, the transport is dominated by the resonant tunneling through the miniband, and the NDR occurs as the miniband breaks into Wannier-Stark ladders with increasing bias. (iii) For higher bias rungs of distinct ladders cross originating new resonances and current peaks. Interestingly, due to the high mobility of the carriers, we obtain low bias NDR peaks with high current densities.

Final remarks

The predicted NDR effects reported here are strictly valid for ballistic electronic transport through ideal aGNR superlattices. For relatively clean systems, however, we expect detrimental effects such as those induced by disorder, impurities and structural defects[23,24,40,41] to broaden the resonances in the I-V curves, thus possibly reducing the peak-to-valley current ratios. Interestingly, a recent calculation for the electronic transport through a single-barrier defined on a zigzag-terminated graphene nanoribbon shows evidence for a transport gap despite the gapless spectrum of the edge states of the system[42]. Therefore, we expect that a superlattice defined on a zigzag graphene nanoribbon should exhibit transport features similar to those of the armchair case investigated here. The effects of edge irregularities, strong disorder and interactions (even at the Hartree level) lie beyond the scope of the present work and deserve further study.

Appendix A: Transfer Matrix

In this Appendix we detail the calculation of the transmission coefficient T_{SD} through the nanoribbon superlattice via the transfer matrix approach. We describe the potential across the system as piecewise constant, Fig.1(b). In each layer the potential is a constant $V_j = V_j^{SL} - eV_{SD}x_j/L$. The superlattice potential V_j^{SL} is 0 for valleys, and $V_b = 230$ mV for barriers (typical value obtained from Refs. 25–28). The second term is the potential energy drop across the jth layers due to the electric field, where x_j is the coordinate of the center of the layer j, and L is the distance between the source and drain.

The solution of the Dirac equation in each layer j ($j =$ S and D for the source and drain, and an integer for the intermediate layers) is given by the plane waves spinors[2,3]

$\psi_{j,n}(x,y) = e^{ik_n y}\varphi_j(x)$. For convenience we write the x-component in a matrix form $\varphi_j(x) = M_j(x)\phi_j$, where the components of the spinor $\phi_j^T = (\alpha_j \ \beta_j)^T$ denote the coefficients of the outgoing and incoming plane waves. The matrix $M_j(x)$ is

$$M_j(x) = \begin{pmatrix} e^{ik_x^{(j)}x} & e^{-ik_x^{(j)}x} \\ s_j e^{ik_x^{(j)}x+i\theta_{j,n}} & -s_j e^{-ik_x^{(j)}x-i\theta_{j,n}} \end{pmatrix}. \quad \text{(A1)}$$

The eigenenergies in each layer are $\varepsilon_{j,n} = V_j + s_j \hbar v_f \sqrt{(k_x^{(j)})^2 + k_n^2}$, with $s_j = +1$ for the conduction band and $s_j = -1$ for the valence band, $k_x^{(j)}$ is the longitudinal momentum in layer j, k_n is the quantized transversal momentum (conserved through the system), and $\theta_{j,n} = \tan^{-1}(k_n/k_x^{(j)})$.

The continuity of the spinors at the interfaces yields $\varphi_j(x_{j,j+1}) = \varphi_{j+1}(x_{j,j+1})$, where $x_{j,j+1}$ is the position of the interface between the layers j and $j+1$. Applying this matching throughout the system, we obtain a 2×2 matrix equation connecting the coefficients from source and drain $\phi_S = T_M \phi_D$, where T_M is the transfer matrix given by

$$T_M = \prod_j M_j^{-1}(x_{j,j+1}) M_{j+1}(x_{j,j+1}). \quad \text{(A2)}$$

The definition of the reflected and transmited waves depends on the sign of the electron energy at source s_S and drain s_D, such that the source and drain coefficients are given by

$$\phi_S^T = \begin{cases} (1 \ r), & \text{if } s_S = +1, \\ (r \ 1), & \text{if } s_S = -1, \end{cases} \quad \text{(A3)}$$

$$\phi_D^T = \begin{cases} (t \ 0), & \text{if } s_D = +1, \\ (0 \ t), & \text{if } s_D = -1. \end{cases} \quad \text{(A4)}$$

From the graphene Dirac hamiltonian, the current density reads $J_x^{(j)} = 4ev_f \varphi_j^\dagger(x)\sigma_x \varphi_j(x)$. At the stationary regime the current flow at source and drain is the same, requiring the match $J_x^S = J_x^D$, from which we identify the transmission coefficient T_{SD},

$$T_{SD}(\varepsilon, k_n, V_{SD}) = |t|^2 \frac{\cos\theta_D}{\cos\theta_S}. \quad \text{(A5)}$$

This transmission coefficient as a function of the energy reveals the electronic structure of the system, in which the confined modes in between the layers show up as resonant spikes and minibands, Fig. 2.

[1] K. S. Novoselov, A. K. Geim, S. V. Morozov, D. Jiang, M. I. Katsnelson, I. V. Grigorieva, S. V. Dubonos, and A. A. Firsov, Nature **438**, 197 (2005).

[2] M. I. Katsnelson, K. S. Novoselov, and A. K. Gaim, Nature Physics **2**, 620 (2006).

[3] A. H. C. Neto, F. Guinea, N. M. R. Peres, K. S. Novoselov, and A. K. Gaim, Rev. Mod. Phys. **81**, 109 (2009).

[4] P. Avouris, Nano letters **10**, 4285 (2010).

[5] M. C. P. Y. Yu, *Fundamentals of Semiconductors* (Springer (Berlin), 2005).

[6] A. Mortazawi, V. P. Kesan, D. P. Neikirk, and T. Itoh, Proc. 19th European microwave conf. **Sept.**, 714 (1989).

[7] T. C. L. G. Sollner, E. R. Brown, W. D. Goodhue, and C. A. Correa, J. Appl. Phys. **64**, 4248 (1988).

[8] K. K. N. S. M. Sze, *Physics of semiconductor devices* (Wiley & Sons (New Jersey), 2007).

[9] R. Tsu, Appl. Phys. Lett. **22**, 562 (1973).

[10] T. C. L. G. Sollner, Appl. Phys. Lett. **43**, 588 (1983).

[11] L. V. Iogansen, Sov. Phys. JETP **18**, 146 (1964).

[12] L. Esaki and R. Tsu, IBM J. Res. Develop. **14**, 61 (1970).

[13] R. Tsu, *Superlattice to Nanoelectronics* (Elsevier (Amsterdam), 2005).

[14] V. J. Goldman, D. C. Tsui, and J. E. Cunningham, Phys. Rev. Lett. **58**, 1256 (1987).

[15] C. Bai and X. Zhang, Physical Review B **76**, 075430 (2007).

[16] L. Brey and H. A. Fertig, Physical Review Letters **103**, 46809 (2009).

[17] C. H. Park, Y. W. Son, L. Yang, M. L. Cohen, and S. G. Louie, Physical Review Letters **103**, 46808 (2009).

[18] M. Barbier, P. Vasilopoulos, and F. M. Peeters, Physical Review B **81**, 075438 (2010).

[19] V. M. Stojanović, N. Vukmirović, and C. Bruder, Physical Review B **82**, 165410 (2010).

[20] P. Burset, A. L. Yeyati, L. Brey, and H. A. Fertig, Physical Review B **83**, 195434 (2011).

[21] X. Guo, D. Liu, and Y. Li, Applied Physics Letters **98**, 242101 (2011).

[22] J. Jiang, J. Wang, and B. Wang, Applied Physics Letters **99**, 043109 (2011).

[23] N. Abedpour, A. Esmailpour, R. Asgari, and M. R. Tabar, Physical Review B **79**, 165412 (2009).

[24] H. Cheraghchi, A. H. Irani, S. M. Fazeli, and R. Asgari, Physical Review B **83**, 235430 (2011).

[25] G. Giovannetti, P. A. Khomyakov, G. Brocks, V. M. Karpan, J. van den Brink, and P. J. Kelly, Phys. Rev. Lett. **101**, 026803 (2008).

[26] M. Vanin, J. J. Mortensen, A. K. Kelkkanen, J. M. Garcia-Lastra, K. S. Thygesen, and K. W. Jacobsen, Phys. Rev. B **81**, 081408(R) (2010).

[27] S. Barraza-Lopez, M. Vanević, M. Kindermann, and M. Y. Chou, Phys. Rev. Lett. **104**, 076807 (2010).

[28] A. Varykhalov, M. R. Scholz, T. K. Kim, and O. Rader, Phys. Rev. B **82**, 121101 (2010).

[29] Z. F. Wang, Q. Li, Q. W. Shi, X. Wang, J. Yang, J. G. Hou, and J. Chen, Appl. Phys. Lett. **92**, 133114 (2008).

[30] V. N. Do and P. Dollfus, J. Appl. Phys. **107**, 063705 (2010).

[31] H. Ren, Q.-X. li, Y. Luo, and J. Yang, Appl. Phys. Lett. **94**, 173110 (2009).

[32] K. Habib, F. Zahid, and R. Lake, Applied Physics Letters **98**, 192112 (2011).

[33] H. Fang, R. Wang, S. Chen, M. Yan, X. Song, and B. Wang, Applied Physics Letters **98**, 082108 (2011).

[34] R. Krahne, A. Yacoby, H. Shtrikman, I. Bar-Joseph, T. Dadosh, and J. Sperling, Appl. Phys. Lett. **81**, 730 (2002).

[35] P. R. Wallace, Phys. Rev. **71**, 622 (1947).

[36] L. Brey and H. A. Fertig, Phys. Rev. B **73**, 235411 (2006).

[37] S. Datta, *Electronic transport in mesoscopic systems* (Cambridge Univ Pr, 1997).

[38] Y. M. Blanter and M. Buttiker, Phys. Rep. **336**, 1 (2000).

[39] B. Trauzettel, D. V. Bulaev, D. Loss, and G. Burkard, Nature Physics **3**, 192 (2007).

[40] M. Han, J. Brant, and P. Kim, Physical review letters **104**, 56801 (2010).

[41] K. Saloriutta, Y. Hancock, A. Kärkkäinen, L. Kärkkäinen, M. J. Puska, and A. P. Jauho, Physical Review B **83**, 205125 (2011).

[42] J. Nakabayashi, D. Yamamoto, and S. Kurihara, Physical Review Letters **102**, 66803 (2009).

[43] D. Dragoman and M. Dragoman, Appl. Phys. Lett. **90**, 143111 (2007).

[44] V. N. Do, Appl. Phys. Lett. **92**, 216101 (2008).

[45] V. N. Do, V. H. Nguyen, P. Dollfus, and A. Bournel, J. Appl. Phys. **104**, 063708 (2008).

[46] A recent work[43] has claimed that low-bias NDR can be achieved with a single barrier in a infinite graphene sheet. This, however, has been disputed in Refs. 44,45.